

**Effect of waveform of the driving field on electroconvection near the dielectric inversion frequency**

K. S. Krishnamurthy\* and Pramoda Kumar†

*Centre for Nano and Soft Matter Sciences, P.O. Box 1329, Jalahalli, Bangalore 560013, India*

(Received 6 November 2015; revised manuscript received 12 January 2016; published 22 February 2016)

This paper concerns the instability behavior of a nematic liquid crystal in the region of dielectric inversion frequency for different waveforms of the exciting electric field. The critical frequency separating the regimes of dielectric and electroconvective primary bifurcation states shows a notable dependence on the waveform. In particular, it is found to undergo a large downshift for square-wave and sawtooth-wave fields as compared to sine-wave and triangle-wave fields. This seems to underscore the significance of harmonics in nonsinusoidal fields for the evolution of patterned electroconvective states. The study also deals with the flow pattern associated with the periodic state and the sequence of secondary instabilities occurring at higher fields to emphasize the role of the Carr-Helfrich mechanism for the instabilities in this region. The relevance of dielectric heating to the formation of transient structures is also pointed out.

DOI: [10.1103/PhysRevE.93.022706](https://doi.org/10.1103/PhysRevE.93.022706)**I. INTRODUCTION**

Nematic electroconvection (EC) driven by the Carr-Helfrich mechanism [1,2] crucially relies, for its occurrence, on the anisotropies of electrical conductivity  $\sigma_a = \sigma_{\parallel} - \sigma_{\perp}$  and dielectric permittivity  $\varepsilon_a = \varepsilon_{\parallel} - \varepsilon_{\perp}$ , the subscripts  $\parallel$  and  $\perp$  denoting the direction relative to the nematic director  $\mathbf{n}$ . For nematic liquid crystals composed of rodlike molecules,  $\sigma_a$  is usually positive [1]. While the sign combination  $(-,+)$  of  $(\varepsilon_a, \sigma_a)$  is known to be ideal for the generation of electric-field-induced periodic space charges leading to sustained cellular flows, EC occurs even in dielectrically positive nematics, provided  $\varepsilon_a$  is sufficiently small [2–4]. Such  $(+,+)$  compounds are particularly interesting since they turn  $(-,+)$  beyond the frequency  $f_i$  at which the relaxation of  $\varepsilon_{\parallel}$  leads to dielectric isotropy. Patterned states found in the vicinity of  $f_i$  are of a different class compared to those formed well below  $f_i$ . In the latter case, below the cutoff frequency  $f_c$  of the conduction regime, the threshold instability is characterized by a periodic quasistationary splay-bend distortion of  $\mathbf{n}$  and oscillation of associated space charges at the frequency of applied field  $f$ . In the dielectric regime beyond  $f_c$ , the opposite situation is obtained. Whereas these two regimes are free from the effects due to dielectric dispersion, the imaginary component of complex permittivity  $\varepsilon''$  becomes relevant to the charge source term in the vicinity of  $f_i$ . The corresponding conductivity anisotropy term  $2\pi f \varepsilon''$  has been incorporated in the early one-dimensional description of EC observed in the dispersion region [5–7]. In later two-dimensional analyses, the periodic instabilities observed near  $f_i$  are considered as predominantly of dielectric origin and interpreted more as modulated Fréedericksz states involving quasistatic domains than as manifestly convective instabilities [8–10].

In most of the previous studies on nematic EC [1], the driving field employed is sinusoidal. However, the threshold characteristics of the instability could show significant

variation with the waveform of the driving field. This was first demonstrated by de Jeu [11] for the classical conduction and dielectric regimes, using square-wave (SQW) and sine-wave (SW) fields; for the roll-state formed below  $f_c$ , the threshold voltage at a given frequency was found to be generally higher for SQW fields than for SW fields, with the difference in threshold being an increasing function of frequency; for the chevron state found above  $f_c$ , the threshold behavior was the opposite. Subsequent one-dimensional analysis predicted the threshold-frequency variation for the SQW field to be sigmoidal, involving bistability in the limiting frequency region of the conduction regime [12], and this was later verified experimentally [13]. According to a two-dimensional linear stability formulation [14], even sinusoidal excitation should involve bistability, though very marginal. More recently, Stannarius and co-workers [15–23] carried out extensive theoretical and experimental studies of electrohydrodynamic excitation of nematics by different waveforms in the frequency region well below dielectric dispersion. One of the results this has led to is the discovery of subharmonic patterned states existing between the conduction and dielectric regimes. The present work concerns electric field experiments conducted in the dielectric relaxation region using different waveforms. In this region, two primary bifurcation states occur, namely, the homogeneous Fréedericksz state and the periodic electroconvective state. The latter, for sine-wave fields, was previously shown [8] to be confined to a narrow frequency band, defined broadly by  $0.8 < f/f_i < 1.4$ . We find the limiting values of the ratio  $f/f_i$  shifting down significantly for both SQW and sawtooth-wave (STW) fields, but remaining practically unchanged for triangle-wave (TW) fields. It is the main purpose here to report these results and highlight the possible effect of higher harmonics of nonsinusoidal fields on the phase diagram in the dielectric dispersion region. We also consider an alternative interpretation based on previous findings relating to the influence of driving waveforms on the instability states in the classical conduction and dielectric regimes [15–23]. This is followed by a discussion of the flow field and then the sequence of secondary instabilities, which together establish the importance of the Carr-Helfrich mechanism for the instabilities close to  $f_i$ .

\*murthyksk@gmail.com

†Present address: Ben-Gurion University of the Negev, Sede Boqer Campus, Israel 8499000.

## II. EXPERIMENT

We have examined the instabilities in butyl *p*-(*p*-ethoxyphenoxy-carbonyl) phenyl carbonate (BEPC) exhibiting an enantiotropic nematic phase between approximately 55 °C and 84 °C. In cooling, the nematic phase persists in the supercooled state down to 35 °C. The sample cells were sandwich type, constructed of indium tin oxide coated glass plates. The electrodes were overlaid with polyimide and buffed unidirectionally to secure planar anchoring. For reference, we take the initial director  $\mathbf{n}_0$  as along  $x$  and the applied field  $E$  normal to the layer as along  $z$ . For BEPC, the static value of  $\varepsilon_a$  was previously measured at 1.592 kHz by de Jeu and Lathouwers [7] and was found to vary from 0.21 at the melting temperature to 0.06 at 84 °C. Our independent measurement at 1 kHz using an Agilent 4284A precision LCR meter agrees with these data to within  $\sim 5\%$ . For our sample,  $\sigma_{\perp}$  varied between 13.9 nS m $^{-1}$  at 40 °C and 72.7 nS m $^{-1}$  at 75 °C; also,  $\sigma_{\parallel}/\sigma_{\perp}$  decreased from 2.76 at 40 °C to 1.16 at 80 °C. For determining the dielectric spectra at various temperatures, we used an HP4194A Impedance/Gain-phase analyzer. For optical observations, a Carl-Zeiss Axio Imager.M1m polarizing microscope equipped with an AxioCam MRc5 digital camera was used. The sample temperature  $\Theta$  was maintained to an accuracy of  $\pm 0.1$  °C by an Instec HCS402 hot stage connected to a STC200 temperature controller. The voltage source was a Stanford Research Systems DS345 function generator coupled to an FLC Electronics voltage amplifier (model A800). The applied voltage was measured with a Keithley-200 multimeter. The voltages given are the rms values unless otherwise stated.

## III. RESULTS AND DISCUSSION

Before dealing with the electrical instabilities in BEPC, it is relevant to mention the frequency and temperature variations of dielectric anisotropy. In view of strongly hindered rotation of molecules around their short axis, as expected,  $\varepsilon_{\parallel}$  relaxes at a much lower frequency than  $\varepsilon_{\perp}$ . The sine-wave frequency dependence of in-phase components on principal permittivities is illustrated in Fig. 1 for two representative temperatures. The frequency of dielectric isotropy  $f_i^S$  (superscript  $S$  indicating sine wave) lies well below the relaxation frequency  $f_R^S$  corresponding to the maximum of the loss component  $\varepsilon''_{\parallel}$ . For example, at 40 °C,  $f_R^S$  is about 62.7 kHz, while  $f_i^S$  is 21.7 kHz. As is evident from Fig. 2,  $f_i^S$  is exponential in  $1/\Theta$ , being given by  $\log_{10} f_i^S = 17.08598 - 3990.37941\Theta^{-1}$ . The activation energy derived from the slope of the linear fit in Fig. 2 is  $\sim 7.9$  eV. It should be mentioned here that de Jeu and Lathouwers [7] were the first to carry out detailed dielectric measurements on several phenyl benzoates (including BEPC) and to report on Debye-type relaxation of  $\varepsilon_{\parallel}$  in these compounds. They found that, in a mixture of phenyl benzoates, both  $\ln f_R(1/\Theta)$  and  $\ln f_i(1/\Theta)$  are linear with the same slope, involving the same activation energy. From  $\ln f_i(1/\Theta)$ , they obtained 8.1 eV as the activation energy for BEPC.

Figure 3 shows the comparative phase behavior of planarly aligned BEPC, in the supercooled nematic state at 40 °C, for various waveforms of frequency  $f \geq 0.5$  kHz. Qualitative features for all the waveforms are similar: In the frequency

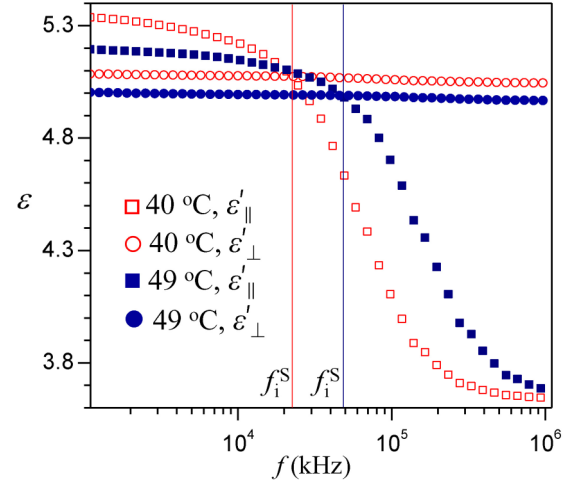


FIG. 1. Typical plots showing the frequency dependence of in-phase permittivity components  $\varepsilon'_{\parallel}$  and  $\varepsilon'_{\perp}$  parallel and perpendicular to the nematic director, respectively. The relaxation of  $\varepsilon_{\parallel}$  leads to a sign reversal of dielectric anisotropy beyond the point  $f_i^S$ .

regime below the critical frequency of the patterned state  $f_P^Y$  ( $Y = S, SQ, ST,$  and  $T$  for sine-, square-, sawtooth-, and triangle-wave fields), the rest state bifurcates into the Fréedericksz state above a threshold  $U_F^Y$  and no secondary bifurcations follow on increasing  $U$ . For  $f \geq f_P^Y$ , the primary instability is characterized by periodic stripes forming at a critical voltage  $U_P^Y$ , with the wave vector along the initial director  $\mathbf{n}_0$ . The periodic instability reveals itself with maximum contrast when the incident light vibration is along  $\mathbf{n}_0$  and it completely disappears for the vibration transverse to  $\mathbf{n}_0$ . Thus the patterned state involves only the splay-bend distortion in the  $xz$  plane, as in classical normal rolls of the conduction regime. However, unlike in the latter case, where the successive real lines are equally spaced, here we have double periodicity or pairing of real lines. This feature, illustrated in Fig. 4 for the SW field, is common to all the waveforms. It indicates a coupling between the periodic EC and homogeneous splay distortion states resulting in the so-called splay rolls (see Fig. 10 in Ref. [4]).

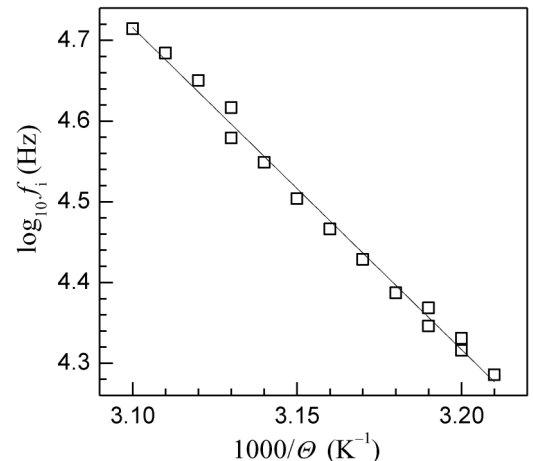


FIG. 2. Dielectric inversion frequency  $f_i$  as a function of  $1/\Theta$  for the BEPC sample used.

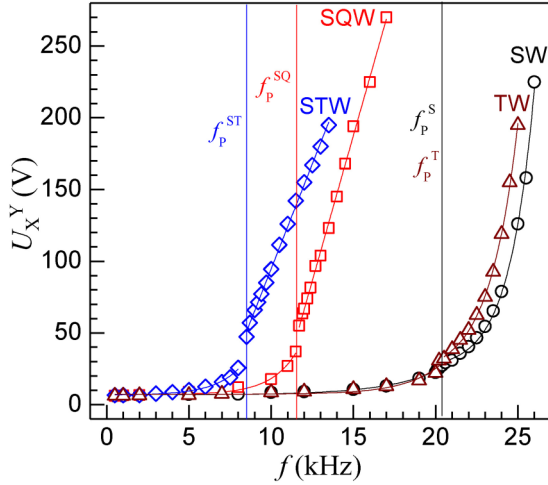


FIG. 3. Frequency variation of the threshold voltage  $U_X^Y$  in a planar 20- $\mu\text{m}$ -thick sample at 40  $^\circ\text{C}$  for different waveforms. In  $U_X^Y$ ,  $X$  denotes the instability state ( $=F$  for Fréedericksz and  $P$  for patterned EC) and  $Y$  denotes the waveform (see the text). For  $f < f_p^Y$ , only the Fréedericksz instability is observed at  $U \geq U_p^Y$ . Similarly, for  $f \geq f_p^Y$ , primary bifurcation into a periodic EC state occurs at threshold  $U_p^Y$ . A slight discontinuity is observed in  $U_X^Y(f)$  at the transition between the Fréedericksz and periodic states.

Our key result concerns variations in  $f_p^Y$ , the lowest or critical frequency at which the EC patterned state is formed from the base state. As is evident in Fig. 3,  $f_p^Y$  exhibits a large downshift for the SQW and STW fields compared to the TW and SW fields. For example, under SW excitation, modulated structures appear at or above a frequency threshold  $f_p^S$  of 20.4 kHz. While the pattern threshold for the TW remains the same as for the SW, it reduces to as low as 11.7 kHz for the SQW and further to 8.7 kHz for the STW. At 40  $^\circ\text{C}$ , as mentioned earlier,  $f_i^S$  is 21.7 kHz, so the ratio  $f_p^S/f_i^S$  is 0.94. Thus, the patterned state sets in at a SW frequency slightly below the dielectric inversion point, as theoretically predicted and observed in other systems [8]. On the other hand,  $f_p^{SQ}/f_i^S$  (for SQW) and  $f_p^{STW}/f_i^S$  (for STW) are unexpectedly low, being about 0.54 and 0.40, respectively. This apparent anomaly could be traced particularly to the harmonics in the immediate neighborhood of the dielectric inversion point. With SQW fields, when the fundamental frequency is 11.7 kHz, all the higher harmonics lie beyond the inversion point  $f_i^S$ . While the nematic is dielectrically unstable at the fundamental frequency far removed from  $f_i^S$ , it

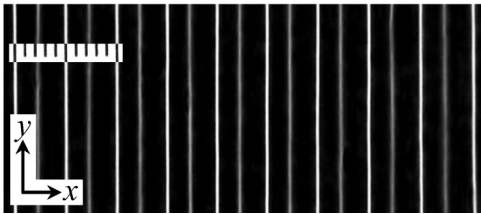


FIG. 4. Pattern of focal lines formed in the sample exposed to a SW field with  $U = 47.4$  V and  $f = 22.5$  kHz. A single polarizer is set along  $x$ . Each scale division is 10  $\mu\text{m}$ .

acquires stability for harmonic waves for which  $\varepsilon_a$  is negative. These opposing effects simultaneously acting on the director may be expected to prevent the dielectric realignment even at voltages well above the threshold for only the fundamental frequency. For example, at 17 kHz, the base state subjected to a SQW field remains unperturbed even at 60 V, but it undergoes dielectric reorientation at less than 10 V under SW excitation. However, at a sufficiently large constraint, the Carr-Helfrich torque due to the anisotropic  $2\pi f \varepsilon''$  term corresponding to the third harmonic of the SQW, being destabilizing in nature, may be expected to generate the patterned instability. Evidently, the importance of higher harmonics decreases with increasing frequency due to the progressive drop in their voltage amplitude. More specifically, the SQW, STW, and TW voltages  $U(t)$  are given, respectively, by the Fourier series expansions

$$U(t) = \frac{4U_0}{\pi} \left( \sin \omega t + \frac{1}{3} \sin 3\omega t + \frac{1}{5} \sin 5\omega t + \dots \right),$$

$$U(t) = \frac{2U_0}{\pi} \left( \sin \omega t - \frac{1}{2} \sin 2\omega t + \frac{1}{3} \sin 3\omega t \mp \dots \right), \quad (1)$$

$$U(t) = \frac{8U_0}{\pi^2} \left( \sin \omega t - \frac{1}{3^2} \sin 3\omega t + \frac{1}{5^2} \sin 5\omega t \mp \dots \right),$$

where  $\omega = 2\pi f$  and  $U_0$  represents the peak voltage in each case. Clearly, the third and higher harmonics of the TW are too low in amplitude relative to the fundamental to be of any significance for the pattern threshold; this explains, qualitatively, why  $f_p^T$  is almost the same as  $f_p^S$ . In both the SQW and STW, the amplitude of the third harmonic relative to the fundamental is the same; the STW has, in addition, the contribution from the relatively strong second harmonic that lies close to but below  $f_i^S$ , or in the dielectrically positive region. The lowest threshold frequency  $f_p^{ST}$  found for the STW is primarily to be attributed to the combined effect of the second and third harmonics.

As mentioned in the Introduction, the dependence of threshold instability characteristics on the nature of the time-varying field  $E(t)$  has been investigated for the conduction and dielectric regimes, employing a wide variety of excitation waveforms [15–23]. However, the conclusions derived thereby cannot be readily transferred to electroconvection around  $f_i$  since, in this case, (i) the space charge generation is mainly through anisotropy of dielectric losses and the usual definition of ionic charge relaxation time as  $\tau_q = \varepsilon_0 \varepsilon_{\perp} / \sigma_{\perp}$  does not apply, (ii) no definitive correspondence is established with the classical regimes based on reversal of either the electric charge distribution or director field, and (iii) the pattern wave number, instead of showing a sudden upward jump as occurs at the transition from the conduction to the dielectric regime, increases continuously with frequency (Fig. 5). In the  $f_i$  region, as analyzed in Ref. [10], while the periodic splay-bend reorientation of the director remains steady, the effective space charge density interacts with the effective field, generating the drag force necessary for convective flows; the charges oscillate at frequency  $f$  but are phase shifted relative to  $E$ . Thus, the EC region beyond  $f_i$  has some resemblance to the normal conduction regime of nematics with  $\varepsilon_a < 0$  [7]. With this in view, we may speculate on the possible

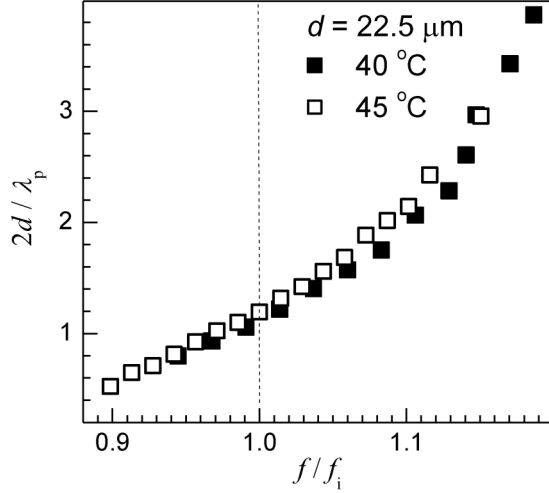


FIG. 5. Wave number (in units of  $\pi/d$ ) of the periodic threshold pattern in BEPC as a function of reduced frequency of the driving sine wave field. The pattern period is  $\lambda_p$ .

implication of earlier dynamical studies to the present work. For illustration, we choose the analysis in Ref. [18] of the instabilities observed under triangular wave excitation. In this case, neutral curves in the voltage-wave number space are found to depend on, among other factors,  $f$  and the waveform asymmetry defined by the parameter  $p = (4T_s/T) - 1$ , with  $T_s$  the time to reach the peak voltage from  $t = 0$  and  $T$ , the period of the waveform. For  $p > 0.76$ , the subharmonic regime in which charge and director fields are of periodicity  $2T$  comes into existence. It exists between the conduction regime terminating at  $f_{c1}$  and the dielectric regime beginning at  $f_{c2}$ , with the interval  $f_{c2} - f_{c1}$  increasing with  $p$ . Importantly, the original cutoff  $f_c$  of the conduction region corresponding to the triangular waveform ( $p = 0$ ) downshifts remarkably to  $f_{c1}$  corresponding to the sawtooth waveform ( $p = 1$ ) (see Fig. 4 in Ref. [18], where  $f_c/f_{c1}$  is about 1.62). We might think of a similar effect as responsible for the relative shift between the threshold curves for sawtooth and triangle waveforms in Fig. 3. However, the large downshift of the SQW threshold curve in Fig. 3 is not explicable by invoking the subharmonic response as it is elicited under the condition  $E(t) \neq -E(t + T/2)$ .

We may think of a straightforward switching application based on the frequency-threshold profiles in Fig. 3. For example, in the frequency region between  $f_p^{SQ}$  and  $f_p^S$ , where the SW-induced dielectric response can lead to near homeotropic reorientation at a sufficiently high voltage, at which the base state is stable for the SQW, switching between the dark and bright states through waveform interchange is feasible. This is most conveniently achieved using a  $90^\circ$ -twisted nematic cell. We have studied the  $U_x^Y(f)$  behavior of BEPC in such a cell and found it to be very nearly the same as depicted in Fig. 3 for untwisted planar cells. The switching performance of the twisted nematic is illustrated in Fig. 6. Essentially, at 17 kHz, we applied a 55-V (peak) SW field to get the dark state in frame  $F_1$ , for the sample between suitably crossed polarizers. Upon switching to the SQW field, the sample reverted to the quiescent state in which, due to the Mauguin waveguiding action, the polarizers in effect became parallel, leading to the

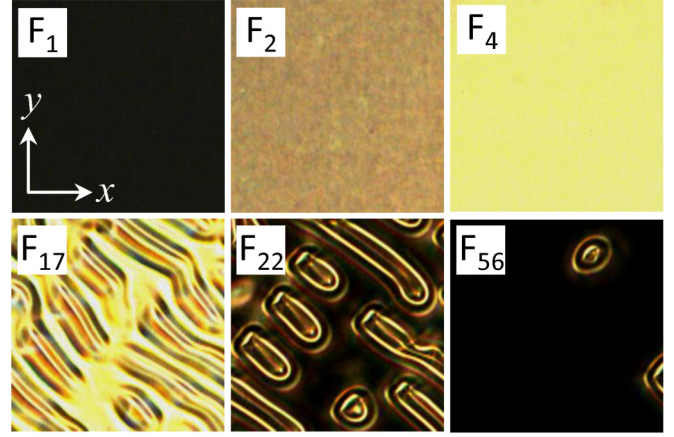


FIG. 6. Switching between dark and bright states in a  $20\text{-}\mu\text{m}$   $90^\circ$ -twisted nematic sample at  $40^\circ\text{C}$ , kept between crossed polarizers with their axes along  $\mathbf{n}_0$  at the entrance and exit planes and subject to a 17-kHz 55-V (peak) field. Here  $F_N$  stands for the  $N$ th frame of the time series with 0.158 s as the interval between successive frames:  $F_1$ , near homeotropic realignment in the SW field;  $F_2$ , partially bright texture soon after switching to the SQW field;  $F_4$ , eventual bright base state texture under the SQW field;  $F_{17}$ , patterned state 0.32 s after switching back to the SW field; and  $F_{22}$ , intermediate loop domain texture before reaching the near dark state in  $F_{56}$ .

bright state in frames  $F_3$  and  $F_4$ . Upon switching back to the SW field, the dark state was recovered, but after a considerable delay due to the formation and slow decay of metastable loop walls, as indicated in frames  $F_{17} - F_{56}$ . At lower frequencies and voltages the delay time could be reduced. Evidently, optimization of switching would require decreasing the layer thickness  $d$  since the transient times may be expected to vary as  $d^2$  [1].

The instability features described for different waveforms (Fig. 3) are observable at all temperatures in the nematic range. For illustration of temperature variation of the pattern threshold, we may compare the data for the SQW and the SW. As depicted in Fig. 7, the critical frequency ratio  $f_p^S/f_p^{SQ}$  shows an overall decrease from about 1.75 to 1.25 as  $\Theta$  is increased from  $40^\circ\text{C}$  to  $70^\circ\text{C}$ . Further, the temperature dependence of  $f_p^S$ , as well as of  $f_p^{SQ}$ , is very well represented by a single-exponential function. As the inset in Fig. 7 shows,  $\ln f_p(1/\Theta)$  is linear for both waveforms, which is a direct consequence of  $f_i(\Theta)$  following the Arrhenius equation. As concerns the dependence of the EC threshold on temperature, the variation for the SW is more pronounced and regular than for the SQW (Fig. 8). Significantly, the temperature coefficients in the two cases are of opposite sign, being positive for the SW. Here  $U_p^S(\Theta)$  is known to be governed by several material parameters. If the critical wave vector at  $f_p^S$  is taken as  $2d$ , from Eq. (30) of Ref. [10], we have

$$U_p^2 = \frac{2\pi^2 K \eta_{\text{eff}}(R + s + 1)}{\varepsilon_0(R + s - 1)\varepsilon_\perp \gamma_1}, \quad (2)$$

where  $K$  is the elastic modulus under one constant approximation,  $\eta_{\text{eff}}$  is the effective flow viscosity,  $\gamma_1$  is the rotational viscosity,  $R = 2\varepsilon_0\pi f_i \varepsilon''/\sigma_\perp$ , and  $s = \sigma'/\sigma_\perp$ , with  $\sigma'$  the real part of complex conductivity parallel to the director. It is known

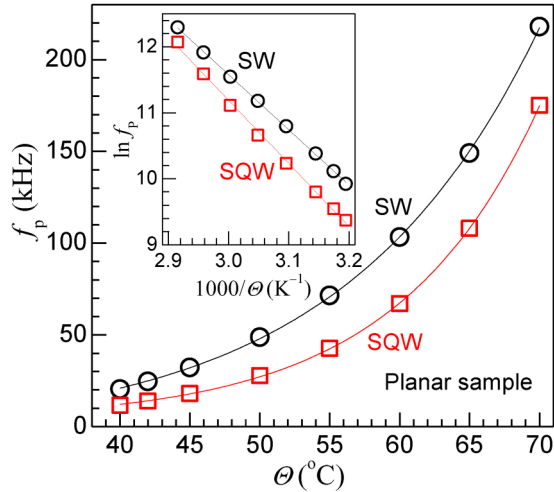


FIG. 7. Temperature variation of the critical frequency  $f_p$  above which the periodic EC state forms as the primary instability. At all temperatures, the critical frequency  $f_p^{\text{SQW}}$  for the SQW is considerably lower than the corresponding frequency  $f_p^{\text{SW}}$  for the SW. Solid lines are exponential fits. The inset shows the linear dependence of  $\ln f_p$  on  $1/\Theta$  ( $\Theta$  being in K) for the two waveforms.

that  $\eta_{\text{eff}}/\gamma_1$  is generally an increasing function of  $\Theta$ , exhibiting a universal variation for calamitics [24];  $1/\varepsilon_{\perp}$  shows a similar trend. These threshold elevating effects under rising  $\Theta$  are partly countered by the decreasing nature of  $K(T)$ . Going by the marked increase in  $U_p$  with  $\Theta$  for the SW, we may surmise the ratio  $(R + s + 1)/(R + s - 1)$  to be an increasing function of  $\Theta$ .

Next we consider the flow field for the periodic state occurring around  $f_i$ . It is relevant to note that there has been no report to date of experimental observation of coherent flows associated with the modulation in the dielectric inversion region. In fact, in Refs. [8,9] the patterned state is taken to be the result of a purely orientational deformation,

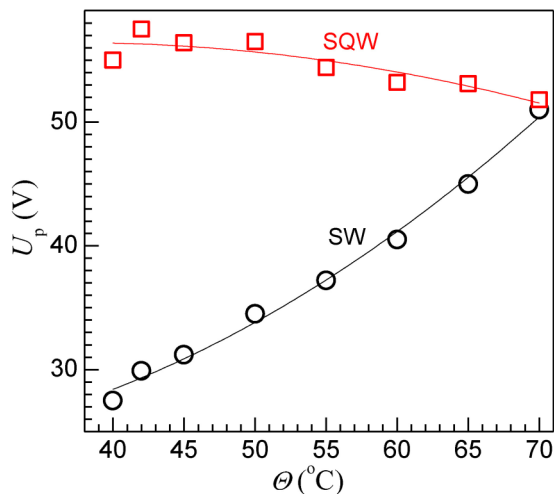


FIG. 8. Temperature variation of the critical voltage  $U_p$  above which the periodic EC state forms as the primary instability. The critical voltage  $U_p^{\text{SW}}$  for the SW approaches the corresponding voltage  $U_p^{\text{SQW}}$  for the SQW as the temperature increases.

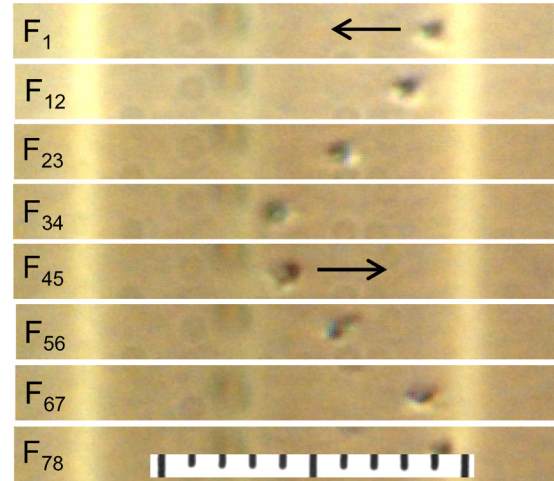


FIG. 9. Tracer particle motion around the vortex axis appearing as oscillatory traverse between adjacent focal lines. Here  $F_N$  refers to the  $N$ th frame of the time series with 0.323 s as the interval between successive frames. The parameters are 70 °C, 52.2 V, 218 kHz, and  $d = 20 \mu\text{m}$ . Parallel polarizers are along  $x$ . Each scale division is 5  $\mu\text{m}$ .

involving no hydrodynamics. This view is later modified in the viscoelastic approach [10], where allowance is made for a steady velocity field of very small amplitude. In a subsequent study [25] demonstrating switchable diffraction gratings based on dielectric sign reversal, the patterned instability near  $f_i$  is described as the Fréedericksz state that is modulated in the plane of the substrates. Experimentally, we find the flow field associated with the modulated state formed around  $f_i$  to be readily observable through the motion of tracer particles immersed in the fluid and the corresponding velocities are not inconsiderable. In Fig. 9, for example, we demonstrate the projected oscillatory motion of a chance particle, which is correlated with the vortical motion of the fluid. In the figure,  $F_N$  denotes the  $N$ th frame of a time series of 200 images captured, with the interval between successive frames being 0.323 s (see Supplemental Material [26] for a movie clip NR.avi of this series that runs at four times the original frame rate). The brighter focal lines are a period  $\lambda_p$  apart and two counterrotating cells exist between them. The in between feeble focal line is shifted slightly to the left of center because of the double periodicity mentioned before. The particle completes one oscillation in about 30 s. If we take the particle as having a diameter of 4  $\mu\text{m}$  and hence orbiting in an ellipse of semimajor and semiminor axes measuring 15 and 8  $\mu\text{m}$ , respectively, the length traversed in a cycle would be about 75  $\mu\text{m}$  corresponding to an average speed of 2.5  $\mu\text{m s}^{-1}$ . In the conduction regime, the speed of flow estimated near threshold is, interestingly, of the same order [27].

The plot in Fig. 10 of the projected position  $s$  of the particle along  $x$  as a function of  $t$  shows some finer features of flow. The velocity component  $v_x$  along  $x$  is expectedly the largest midway between the turning points. The times for forward ( $A$  to  $B$ ) and reverse ( $B$  to  $C$ ) motions are consistently different, pointing to dissimilar conditions at the two substrates.

On slowly increasing  $U$  at  $f < f_i$ , the normal roll state, with the threshold control parameter  $\Sigma_p = [(U/U_p)^2 - 1] = 0$ ,

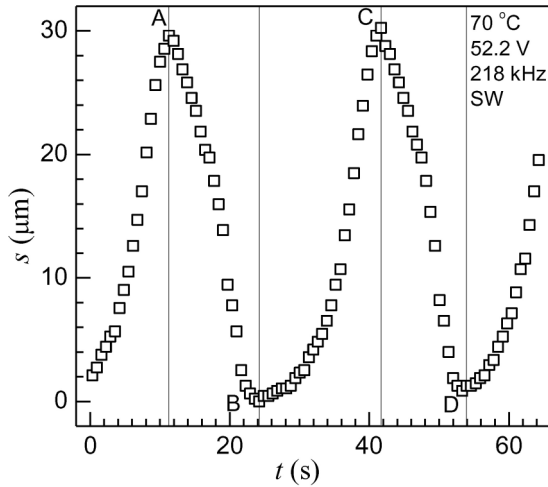


FIG. 10. Position along  $x$  of a particle revolving around the axis of a flow cell as a function of time.

undergoes a regular sequence of symmetry-breaking transitions into various stationary structures prior to the eventual onset of the Fréedericksz instability. In Fig. 11, which exemplifies this feature, the transformation from the normal to oblique or zigzag roll state via the undulatory instability, as in Figs. 11(a)–11(d), has a striking resemblance to a similar occurrence in the classical conduction regime, above the Lifshitz frequency [28]. Just as in the latter case, the streamlines for the undulatory and oblique roll states here are observed to be helical as in Fig. 12 (see Supplemental Material [26] for a movie clip OR.avi on helical motion that runs at 12 times the original frame rate).

For a large control parameter, the original splay-bend structure develops a twist component that is opposite in sense for the zig and zag sections [29]. The kinks separating these straight sections involve line singularities, which appear as bright points in Figs. 11(e) and 11(f). This is followed by the rolls turning into Brochard-Leger walls [30], as in

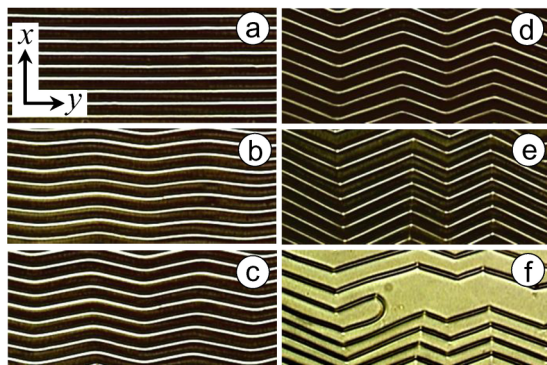


FIG. 11. Focal lines corresponding to (a) normal rolls at  $\Sigma = 0.13$ , (b) undulatory rolls at  $\Sigma = 0.22$ , (c) undulatory rolls of increased amplitude at  $\Sigma = 0.23$  V, (d) zigzag Williams-like rolls at  $\Sigma = 0.37$ , (e) zigs and zags separated by disclinations at  $\Sigma = 0.57$ , and (f) hybrid state formed during transformation of rolls into Fréedericksz loop walls at  $\Sigma = 0.89$ . Here  $f_p^S/f_i^S = 0.89$ . Parallel polarizers are along  $x$ .

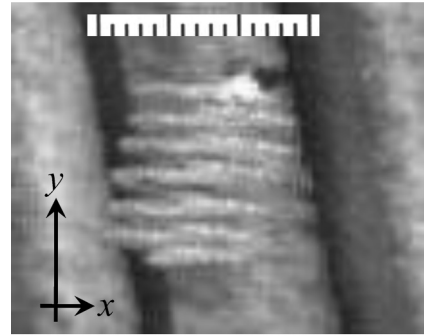


FIG. 12. Helical motion of a tracer particle in the oblique roll state viewed by  $z$  stacking of 600 images recorded over 148 s. The image is inverted to enhance the visibility of the spiral trajectory between the inclined focal lines now appearing dark. The axis of the helix is at a slight angle to the vertical ( $y$ ) due to a slow drift of the pattern to the left. Each scale division is  $2 \mu\text{m}$ . The parameters are  $60^\circ\text{C}$ ,  $107 \text{ kHz}$ , and  $\Sigma = 0.23$ .

Fig. 11(f), and in the final stages leading to the homogeneous Fréedericksz state, metastable loop walls with opposite kinks along the easy axis are obtained. Far from  $f_i$ , where the pattern period is small, higher-order instabilities manifest first as oscillatory EC domains and then as highly dynamic chevrons. In Figs. 13(a)–13(d), depicting the chevrons formed at various voltages at a given frequency, the progressive increase in chevron angle with  $\Sigma$  is evident. Notably, at such large values of  $f$  and  $\Sigma$  corresponding to Fig. 13(d), the attendant dielectric heating [31] elevates  $f_i$  to a value above the applied frequency so that the chevron state gives way to the Fréedericksz instability. This transition occurs via several intermediate states involving bimodal structures. In Fig. 13(e)

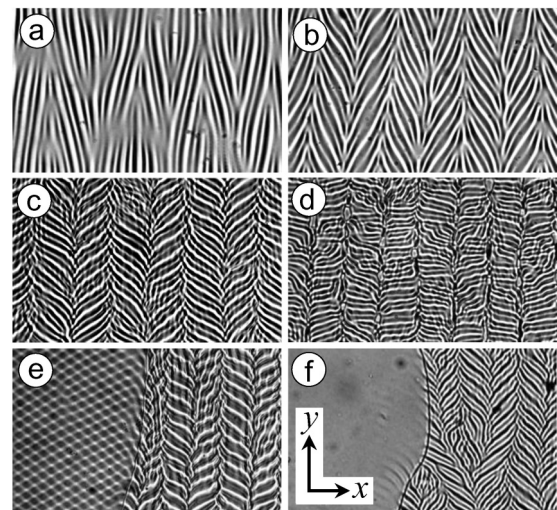


FIG. 13. (a) and (d) Chevron states for  $f/f_i = 1.13$  showing increasing chevron angle with control parameter.  $\Sigma$ -values are (a) 0.37, (b) 0.81, (c) 1.26, and (d) 1.31. (e) and (f) Transformation of the chevron state to the Fréedericksz state at  $\Sigma = 1.44$ , consequent on a change in the sign of  $\epsilon_a$  (or upward shift of  $f_i$ ) due to dielectric heating. In (e), the region on left shows the transient bimodal state; eventually, as can be seen on the left in (f), the uniform Fréedericksz state is established all over.

illustrating this feature, the bimodal pattern in the left half decays with the passage of time, resulting in the homogeneous Fréedericksz texture that is shown in Fig. 13(f). A comparison between the chevron textures in the right half of Figs. 13(e) and 13(f) shows how the chevron angle decreases as the transition to the homogeneous state is approached. This is explicable by the decrease in effective  $\Sigma$  during heating. The minimum increase in temperature that would induce the transition to the Fréedericksz state could be estimated by setting  $f/f_i^S = 1$ . From the  $f_i^S(\Theta)$  relation mentioned previously, the increase in  $\Theta$  here is by 1.5 °C. These high-frequency thermal effects have not been previously considered in textural studies at frequencies near  $f_i^S$  [32].

#### IV. CONCLUSION

In the present study, we have focused on EC that involves charges created via dielectric loss and occurs in a narrow frequency band around the dielectric inversion point  $f_i$ , within which the sign of  $\varepsilon_a$  changes. The results demonstrate the importance of the driving waveform in the evolution of EC states around  $f_i$ . In particular, the frequency band of EC is found to exhibit a large downshift for square-wave and sawtooth-wave fields relative to sine-wave and triangle-wave fields. This implies a corresponding shift in the effective

relaxation frequency for SQW and STW fields. In consequence, a planar nematic layer exposed to a SQW or STW field exhibits dielectric stability at such high voltages as will, under a SW or TW field, render the layer almost completely homeotropic. In addition, the experiments here clearly reveal the elliptical and helical streamlines associated, respectively, with normal and oblique splay rolls formed at or near  $f_i^S$ . This, together with the sequence of secondary bifurcations identified herein, points to the likeness of the instabilities to those occurring in the classical conduction and dielectric regimes. An additional interesting feature recognized is the evolution of two-dimensional patterns in the course of transition from the dielectrically negative state to the positive state occasioned by dielectric heating. Overall, the results underscore the need for a theoretical analysis of the EC instability under nonsinusoidal excitation, taking into account the contribution of dielectric loss to space charge generation. Experiments on spatiotemporal features of distortion (using high-speed image acquisition as in, for example, Ref. [18]) are also of interest in exploring the dynamical aspects of the instability states and their dependence on the excitation waveform.

#### ACKNOWLEDGMENT

We are grateful to Professor G. U. Kulkarni for experimental facilities and encouragement.

- 
- [1] L. M. Blinov and V. G. Chigrinov, *Electrooptic Effects in Liquid Crystal Materials* (Springer, Berlin, 1994).
- [2] E. Bodenschatz, W. Zimmermann, and L. Kramer, *J. Phys. (Paris)* **49**, 1875 (1988).
- [3] B. Dressel and W. Pesch, *Phys. Rev. E* **67**, 031707 (2003).
- [4] P. Kumar and K. S. Krishnamurthy, *Phys. Rev. E* **74**, 031705 (2006).
- [5] W. H. de Jeu, C. J. Gerritsma, P. Van Zenten, and W. J. A. Goossens, *Phys. Lett. A* **39**, 355 (1972).
- [6] W. J. A. Goossens, *Phys. Lett. A* **40**, 95 (1972).
- [7] W. H. de Jeu and T. W. Lathouwers, *Mol. Cryst. Liq. Cryst.* **26**, 225 (1974); **26**, 235 (1974).
- [8] V. G. Chigrinov, T. V. Korkishko, M. I. Barnik, and A. N. Trufanov, *Mol. Cryst. Liq. Cryst.* **129**, 285 (1985).
- [9] M. I. Barnik, L. M. Blinov, A. N. Trufanov, V. G. Chigrinov, and T. V. Korkishko, *Sov. Phys. JETP* **60**, 113 (1985).
- [10] V. G. Chigrinov, A. Sparavigna, and A. Strigazzi, *Phys. Rev. E* **53**, 4918 (1996).
- [11] W. H. de Jeu, *Phys. Lett. A* **37**, 365 (1971).
- [12] E. Dubois-Violette, *J. Phys. (Paris)* **33**, 95 (1972); I. W. Smith, Y. Galerne, S. T. Lagerwall, E. Dubois-Violette, and G. Durand, *J. Phys. (Paris) Colloq.* **36**, C1-237 (1975).
- [13] Orsay Liquid Crystal Group, *Phys. Lett. A* **39**, 181 (1972).
- [14] H. M. Zenginoglou, R. A. Rigopoulos, and I. A. Kosmopoulos, *Mol. Cryst. Liq. Cryst.* **39**, 27 (1977).
- [15] T. John, U. Behn, and R. Stannarius, *Eur. Phys. J. B* **35**, 267 (2003).
- [16] H. Amm, M. Grigutsch, and R. Stannarius, *Z. Naturforsch. A* **53a**, 117 (1998).
- [17] T. John and R. Stannarius, *Phys. Rev. E* **70**, 025202(R) (2004).
- [18] T. John, J. Heuer, and R. Stannarius, *Phys. Rev. E* **71**, 056307 (2005).
- [19] R. Stannarius, J. Heuer, and T. John, *Phys. Rev. E* **72**, 066218 (2005).
- [20] C. Bohley, J. Heuer, and R. Stannarius, *J. Opt. Soc. Am. A* **22**, 2818 (2005).
- [21] J. Heuer, T. John, and R. Stannarius, *Mol. Cryst. Liq. Cryst.* **449**, 11 (2006).
- [22] J. Heuer, T. John, and R. Stannarius, *Phys. Rev. E* **78**, 036218 (2008).
- [23] D. Pietschmann, T. John, and R. Stannarius, *Phys. Rev. E* **82**, 046215 (2010).
- [24] F.-J. Bock, H. Knepe, and F. Schneider, *Liq. Cryst.* **1**, 239 (1986).
- [25] S. W. Kang, S. Sprunt, and L. C. Chien, *Appl. Phys. Lett.* **78**, 3782 (2001).
- [26] See Supplemental Material at <http://link.aps.org/supplemental/10.1103/PhysRevE.93.022706> for movie clips (NR.avi and OR.avi) showing the motion of tracer particles in the normal and oblique roll states. Further details are provided in the text file of this section.
- [27] A. Joets and R. Ribotta, *J. Phys. (Paris)* **47**, 595 (1986).
- [28] R. Ribotta, A. Joets, and L. Lei, *Phys. Rev. Lett.* **56**, 1595 (1986).
- [29] A. de Lozar, W. Schopf, I. Rehberg, D. Svensek, and L. Kramer, *Phys. Rev. E* **72**, 051713 (2005).
- [30] F. Brochard, *J. Phys. (Paris)* **33**, 607 (1972); L. Leger, *Mol. Cryst. Liq. Cryst.* **24**, 33 (1973).
- [31] Y. Yin, S. V. Shiyankovskii, and O. D. Lavrentovich, *Phys. Rev. Lett.* **98**, 097801 (2007).
- [32] S. W. Kang and L. C. Chien, *Macromol. Res.* **15**, 396 (2007).